Atmos. Meas. Tech., 8, 4265–4280, 2015
www.atmos-meas-tech.net/8/4265/2015/
doi:10.5194/amt-8-4265-2015


Atmospheric Measurement Techniques
Open Access

# A new method for the absolute radiance calibration for UV–vis measurements of scattered sunlight

**T. Wagner**[1], **S. Beirle**[1], **S. Dörner**[1], **M. Penning de Vries**[1], **J. Remmers**[1], **A. Rozanov**[2], **and R. Shaiganfar**[1]

[1]Max-Planck-Institute for Chemistry, Mainz, Germany
[2]Institute for Environmental Physics, University of Bremen, Bremen, Germany

*Correspondence to:* T. Wagner (thomas.wagner@mpic.de)

Received: 30 March 2015 – Published in Atmos. Meas. Tech. Discuss.: 28 May 2015
Revised: 22 September 2015 – Accepted: 24 September 2015 – Published: 14 October 2015

**Abstract.** Absolute radiometric calibrations are important for measurements of the atmospheric spectral radiance. Such measurements can be used to determine actinic fluxes, the properties of aerosols and clouds, and the shortwave energy budget. Conventional calibration methods in the laboratory are based on calibrated light sources and reflectors and are expensive, time consuming and subject to relatively large uncertainties. Also, the calibrated instruments might change during transport from the laboratory to the measurement sites. Here we present a new calibration method for UV–vis instruments that measure the spectrally resolved sky radiance, for example zenith sky differential optical absorption spectroscopy (DOAS) instruments or multi-axis (MAX)-DOAS instruments. Our method is based on the comparison of the solar zenith angle dependence of the measured zenith sky radiance with radiative transfer simulations. For the application of our method, clear-sky measurements during periods with almost constant aerosol optical depth are needed. The radiative transfer simulations have to take polarisation into account. We show that the calibration results are almost independent from the knowledge of the aerosol optical properties and surface albedo, which causes a rather small uncertainty of about < 7 %. For wavelengths below about 330 nm it is essential that the ozone column density during the measurements be constant and known.

## 1 Introduction

Measurements of the spectrally resolved sky radiance are important for many atmospheric remote-sensing applications in atmospheric chemistry and physics. They are also useful for the quantification of the energy yield of photovoltaic cells or doses of harmful UV radiation. Possible applications include the following:

- Improvement of aerosol retrievals from multi-axis differential optical absorption spectroscopy (MAX-DOAS) observations (Hönninger et al., 2002): if the measured radiances are absolutely calibrated, they do not have to be normalised by zenith sky observations. This allows e.g. to better constrain the total aerosol optical depth (AOD).
- Improved quantification of the aerosol absorption: usually the sensitivity of MAX-DOAS retrievals to the aerosol single-scattering albedo is rather weak. Here measurements of the absolute radiances may help to separate aerosol absorption from extinction.
- Better cloud characterisation: the brightness of clouds at the bottom or the sides depends on their optical depth, shape and internal structure. Absolute radiances measured at various angles can be quantitatively compared with results from 3-D cloud models to constrain the cloud properties.
- Extraction of well-calibrated colour index values: from radiometrically calibrated spectra, colour indices can be extracted, which can be directly compared to the results from radiative transfer models.
- Estimation of actinic fluxes: from absolutely calibrated MAX-DOAS spectra taken at different elevation angles (and possibly also different azimuth angles), the spectrally resolved actinic flux over the observed wavelength range can be estimated.

– Estimation of UV doses at the surface: from absolutely calibrated MAX-DOAS measurements (or other measurements covering multiple viewing directions) the UV fluxes at the surface can be estimated. Here it should, however, be noted that a constant and known $O_3$ column during the measurements is a prerequisite for an accurate radiometric calibration in the UV-B spectral range (315–280 nm).

– Quantification of the radiation budget: from absolutely calibrated MAX-DOAS spectra in the UV, visible and near-IR spectral range, the amount of the downward shortwave radiation can be calculated.

– Estimation of the energy yield of photovoltaic cells. Here measurements of the angular distribution of the sky radiance are important for photovoltaic cells, which are not directly opposed to the direct sunlight. But also for photovoltaic cells opposed to the direct sunlight, the yield resulting from the diffuse radiation can be significant (especially for high aerosol loads).

Absolutely calibrated measurements of the sky radiance are usually elaborate and complex, because the calibration is performed in a laboratory using e.g. calibrated light sources and reflecting surfaces. Also the errors of the radiometric calibration can be quite large: typical uncertainties of the calibration procedures for atmospheric radiance measurements are reported to range from 3 to 10 % (Pissulla et al., 2009). From comparison exercises during field campaigns even larger differences between individual instruments have been reported (up to 33 %; see Pissulla et al., 2009). Here it is interesting to note that measurements of the solar irradiance usually show much better agreement (e.g. Wuttke et al., 2006).

In this study we present a new method for the absolute radiometric calibration of instruments that observe spectrally resolved scattered sunlight, which is completely independent from laboratory measurements. Instead it is based on the comparison of measurements of scattered sunlight under well-defined conditions with radiative transfer simulations. In particular the dependence of the observed zenith sky radiance on the solar zenith angle (SZA) is investigated. Here it is interesting to note that typical (MAX-)DOAS instruments have rather small fields of view (usually about 1°), but also measurements with larger fields of view could in principle be used as long as the correct field of view is considered in the radiative transfer simulations.

Continuous measurements during a couple of hours on one day are sufficient for the application of our method.

The new calibration method is particularly suitable for DOAS measurements (Platt and Stutz, 2008). DOAS measurements of direct or scattered sunlight in the UV, visible and near-IR spectral range are widely used to identify and quantify spectral absorption features of atmospheric trace gases. DOAS instruments are usually not radiometrically calibrated, because the DOAS technique is sensitive to differential absorption structures and does not require absolute calibration. But some of the data products derived from DOAS observations (see above) can be improved if radiometrically calibrated DOAS instruments are used. Our new method can also be applied to other measurements of scattered sunlight (e.g. spectroradiometer or sun photometer measurements). Here it should be noted that our method cannot be applied to irradiance measurements, because for such measurements the relative dependence of the observed irradiance on SZA hardly changes with the aerosol load and properties (except for very high aerosol loads).

The paper is organised as follows: in Sect. 2 the data sets used in our study (MAX-DOAS measurements and radiative transfer simulations) are introduced. Section 3 presents the application of the method together with an estimation of the uncertainties. Also the effects of (neglecting) polarisation and rotational Raman scattering are discussed. Section 4 presents the conclusions.

## 2 Data sets

### 2.1 MAX-DOAS measurements

We use MAX-DOAS observations performed during the Cabauw Intercomparison Campaign of Nitrogen Dioxide measuring Instruments (CINDI) in summer 2009 (Piters et al., 2012). They have already been described in Roscoe et al. (2010) and Wagner et al. (2014), but the most important measurement properties are briefly described below: our instrument is a so-called Mini-MAX-DOAS instrument covering the wavelength range from 312 to 458 nm with a spectral resolution between 0.45 and 0.8 nm (see Fig. A1 in the Appendix). The typical integration time is 1 min; the field of view is $\sim 1.2°$. During the CINDI campaign, measurements with our instrument in exact zenith view (90° elevation angle) were not possible, because the instrument was operated close to a tall tower. Thus we used measurements made in near-zenith direction at an elevation angle of 85°. The viewing azimuth direction was towards west-northwest (287° with respect to north). The measured light is transferred via a 1.5 m long wound-up quartz fibre to a temperature-stabilised miniature spectrometer (Ocean Optics USB2000) and recorded by a one-dimensional CCD detector (Sony ILX511). Because of the transmission through the quartz fibre, the polarisation sensitivity of the instrument is negligible. The detector signal is expressed as detector readout per time (counts per second). The optical throughput of the instrument is not known, since it depends on the efficiencies of the detector, the diffraction grating, a tilted mirror, a glass fibre and the telescope lens.

For this study, radiances are extracted from the measured spectra for discrete wavelengths ranging from 315 to 455 nm in intervals of 10 nm. The extracted radiances are calculated

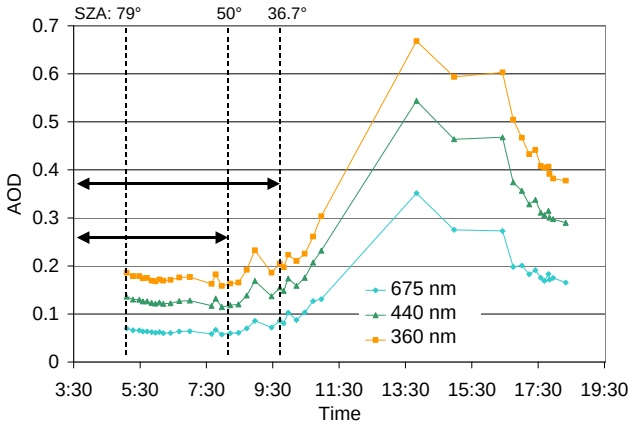


**Figure 1.** AOD derived from sun photometer observations (AERONET) at Cabauw at three wavelengths. The black vertical lines indicate the start of the AERONET measurements (05:06, SZA: 79° ) and the ends of the two measurement periods used in this study: 03:30–08:05 (SZA: 90–50°); 03:30–09:41 (SZA: 90–36.7°).

as averages over seven detector pixels ($\sim 0.5$ nm) around the selected wavelengths. Here it should be noted that our choice of wavelengths was arbitrary and that a different (e.g. finer) wavelength grid could be used as well (e.g. if the detector sensitivity changes rapidly with wavelength).

We applied our method to measurements made on the morning of 24 June 2009. This morning was completely cloud-free as indicated by a ground-based digital camera (with images taken every 10 min) as well as by a backscatter lidar (see Wagner et al., 2014). The aerosol optical depth (AOD) was low and constant throughout most of the morning according to sun photometer measurements; see Fig. 1. After about 10:00 UT the AOD increased, and clouds appeared around noon (Wagner et al., 2014). In a first attempt we used all measurements between 03:00 and 09:41, representing a SZA range between 90 and 37°. During the analysis, however, it turned out that the calibration results significantly improved if only measurements before 08:05 (SZA $\sim 50°$) were used (see Sect. 3). This finding is probably related to the smaller variation of the AOD before $\sim$ 08:00. In addition, the exclusion of small scattering angles might play a role. Both time periods are indicated by the black arrows in Fig. 1.

### 2.2 Radiative transfer simulations

Radiances are simulated with the full spherical Monte Carlo Radiative Transfer Inversion Model (McArtim; Deutschmann et al., 2011). The model output can be generated in scalar or vector mode. Also the effect of rotational Raman scattering (RRS) can be considered. In most simulations we considered polarisation, but we did not consider RRS (see details below). The specific parameters for Rayleigh (and rotational Raman) scattering are adapted from Landgraf et al. (2004). The parameterisation of the anisotropy of the polarisability is based on Chance and Spurr (1997). The output of the model is the normalised radiance (also referred to as atmospheric transmittance):

$$R_{\mathrm{norm}}(\lambda) = \frac{R(\lambda)}{I(\lambda)}. \quad (1)$$

Here $R$ is the radiance (e.g. in units of W m$^{-2}$ nm$^{-1}$ sr$^{-1}$) and $I$ is the solar irradiance (e.g. in units of W m$^{-2}$ nm$^{-1}$). It depends on the viewing geometry, wavelength, field of view and spectral resolution of the instrument. To obtain the radiance from the model output, the normalised radiance has to be multiplied by the solar irradiance.

$$R(\lambda) = I(\lambda) \cdot R_{\mathrm{norm}}(\lambda) \quad (2)$$

Here we use a solar irradiance spectrum from Chance and Kurucz (2010), which has an accuracy of about 1 % according to a study by Thuillier et al. (2004). Before it is applied to Eq. (2) it is multiplied by 0.969 to account for the effect of the changing sun–earth distance (during our measurement the sun–earth distance is 1.6 % larger than for the measurement of the sun irradiance spectrum). Here it is interesting to note that changes of the solar irradiance during the solar cycle are rather small. Haigh et al. (2010) studied the changes between 2004 and 2007 for the declining phase of the solar cycle (from shortly after the maximum of cycle 23 to close to the subsequent minimum) and found variations < 1 % for wavelengths > 350 nm. For shorter wavelengths the uncertainties slightly increase (for 315 nm they are about 1.5 %). Similar differences are expected for our measurements, which were taken at the minimum between solar cycle 23 and 24, while the solar spectrum used here was scaled to a measurement taken in 1992, shortly after the maximum of solar cycle 22. Here it should be noted that several solar irradiance spectra are available and are described in the scientific literature (see e.g. also Bernhard et al., 2004). But it is beyond the scope of this study to comment on the possible advantages or disadvantages of the different solar spectra. It should, however, be noted that the uncertainties of the derived radiance calibration will directly be proportional to the uncertainties of the used solar spectrum.

In the next step the solar irradiance spectrum is convolved with the slit function of our instrument (see Fig. 2) to make the simulation results directly comparable to the measured radiances. In addition to the convolution, averages of the simulated radiance over intervals of 0.5 nm around the selected wavelengths are calculated to exactly match the radiances of the measured spectra (see Sect. 2.1). Here, in particular the following points are important:

a. To achieve consistency between the wavelength calibrations of the measured and simulated spectra, the spectral calibration of the measured spectrum should be performed by fitting the measured spectrum against the convolved solar irradiance spectrum.

**Table 1.** Overview on the different scenarios (for detailed description see Sect. 2.2). For all scenarios radiances are simulated for AOD between 0 and 0.5.

| Scenario | Description |
|---|---|
| Standard (std) | Standard scenario: aerosol properties: HG phase function with asymmetry parameter of 0.68; layer: 0–1 km; single-scattering albedo: 0.95; surface albedo: 0.05; temperature, pressure and $O_3$ profiles from the US Standard Atmosphere, polarisation but no Raman scattering taken into account. |
| Scenario | Deviation from standard scenario |
| AP 0.60 | HG phase function with asymmetry paramater of 0.60 |
| AP 0.75 | HG phase function with asymmetry paramater of 0.75 |
| AP 0.85 | HG phase function with asymmetry paramater of 0.85 |
| Mie 500 | Mie phase function for size distribution with maximum at 500 nm and standard deviation of ±50 %; real refractive index: 1.34 |
| Mie 1000 | Mie phase function for size distribution with maximum at 1000 nm and standard deviation of ±50 %; real refractive index: 1.34 |
| SSA 0.80 | Single-scattering albedo: 0.80 |
| SSA 0.90 | Single-scattering albedo: 0.90 |
| SSA 1.00 | Single-scattering albedo: 1.00 |
| 0–2 km | Aerosol layer height: 2 km |
| Albedo 0.03 | Surface albedo: 0.03 |
| Albedo 0.07 | Surface albedo: 0.07 |
| Albedo 0.10 | Surface albedo: 0.10 |
| Albedo SZA dep. | SZA-dependent surface albedo (see text) |
| Ring | Including Raman scattering |
| $NO_2$ | Including $NO_2$ absorption (see text) |
| strat. aerosols | Including stratospheric aerosols (see text) |
| $T$ and $p$ | Using temperature and pressure profiles for Cabauw |
| Cabauw | Including Raman scattering, $NO_2$ absorption and stratospheric aerosols, and using temperature and pressure profiles for Cabauw |

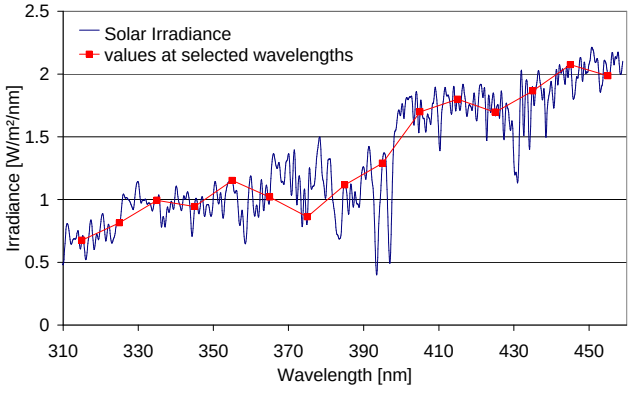


**Figure 2.** Convolved solar irradiance spectrum (blue line) and extracted radiances at the specific wavelengths selected in this study.

b. The spectral convolution of the solar irradiance spectrum should be performed using a slit function which matches that of the measured spectra. We determined the slit function of our instrument by fitting the convolved high-resolution solar spectrum (step a) to the measured spectra. During the fit process the full width at half maximum (FWHM) of the Gaussian convolution kernel is varied until best agreement is found. The derived FWHM ranges between about 0.80 at 315 nm and 0.45 at 355 nm. We used the wavelength-dependent FWHM for the convolution of the high-resolution solar spectrum. The temporal variation of the FWHM during the period of our measurements is < 1 %.

c. The extracted irradiance should be averaged over the same interval as that over which the measured radiance is extracted (in this study seven detector pixel corresponding to about 0.5 nm).

Small deviations from this procedure can lead to large errors of the simulated radiances. For example, a spectral shift of 0.2 nm can cause deviations of the extracted irradiances of up to 16 % for the wavelengths selected in this study.

For the simulations we defined several scenarios with different atmospheric and surface properties. In addition, we performed simulations considering or not considering polarisation and rotational Raman scattering. The different scenarios are summarised in Table 1. For all scenarios radiances are simulated for AOD ranging from 0 to 0.5 (0, 0.02, 0.05, 0.1, 0.15, 0.2, 0.3, 0.4, 0.5). The viewing angle, SZA, and relative azimuth angle used in the simulations were adapted to each

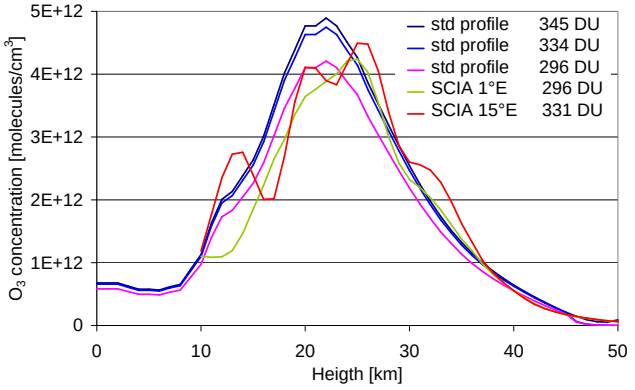


**Figure 3.** Comparison of different ozone profiles for the day of our measurements. The standard profile used in our simulations (345 DU) is shown together with two measured profiles from SCIAMACHY (55.62° N, 1.00° E: 296 DU; 53.89° N, 15.26° E: 331 DU). In addition, two scaled standard profiles matching the same $O_3$ VCD as the SCIAMACHY profiles are shown.

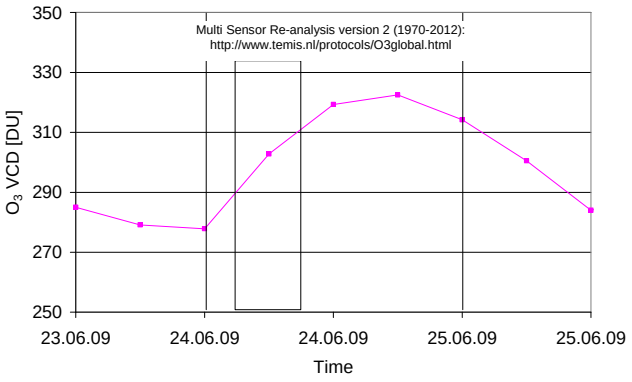


**Figure 4.** Time series of the $O_3$ vertical column density (VCD) from above Cabauw during the period of our measurements (indicated by the black rectangles).

individual measurement. The radiances are simulated for a FOV of 1.2°.

### 2.2.1 Ozone absorption

An important aspect of the radiative transfer simulations at short wavelengths (below about 330 nm) is to consider the correct ozone column density for the day of the measurements. Unfortunately, it turned out that the $O_3$ column density strongly changed during the period of our measurements (from about 290 to 310 DU), and strong horizontal gradients were also present (see Figs. 3 and 4). Thus radiative transfer simulations using a single ozone profile (in our simulations we used a profile from the US Standard Atmosphere; see Fig. 4) cannot well describe the radiances below 330 nm for the complete period of the measurements, and accordingly our calibration results for these wavelengths (covering the important UV-B spectral range) have to be interpreted with caution.

For our simulations we used an ozone profile from the US Standard Atmosphere (United States Committee on Extension to the Standard Atmosphere, 1976) with an $O_3$ VCD of 345 DU (see Fig. 3). Later it turned out that two measured ozone profiles close to the measurement site were available from SCIAMACHY limb observations (Sonkaew et al., 2009). These profiles showed smaller $O_3$ VCDs: 296 and 331 DU (Fig. 3). The rather large difference between the two neighbouring $O_3$ profiles indicates strong horizontal gradients close to Cabauw on that day. These gradients are also indicated by the strong temporal variation of the $O_3$ VCD (see Fig. 4).

The radiances simulated for the different $O_3$ profiles are shown in Fig. A2. The largest differences are found at short wavelengths and for small SZAs. For these SZAs the variation of the $O_3$ VCD has a strong impact on the radiances, while the influence of the profile shape is relatively small. In contrast, for SZA close to 90° the relative profile shape has a strong effect on the relative difference of the simulated radiances (Umkehr effect; see Götz et al., 1934). This is, however, not important for our study, because our calibration method is sensitive to the absolute differences between the measured and simulated radiances (see Sect. 3). Because of the strong temporal variation and the large spatial gradients of the $O_3$ VCD on the day of our measurements, we did not update our simulation results with one of the measured SCIAMACHY profiles. We do not expect much improvement to the results in the presence of such strong gradients, even if a more appropriate profile (e.g. from SCIAMACHY) were to be used.

From the measurements used in our study (which represent a rather extreme situation with a relative change of the ozone VCD of about 5 % within 3 h) we cannot further explore the potential and accuracy of our calibration method in the UV-B spectral range in a meaningful way. Nevertheless, we expect that in the UV-B spectral range similar accuracies as for the larger wavelengths could in principle be obtained, because usually the thickness of the ozone layer is well known from independent observation. Satellite observations have an accuracy of about 1–2 % (e.g. Loyola et al., 2011). Here it should be noted that in principle the ozone VCD can also be derived from the DOAS measurement itself, but usually the ozone VCD is no standard retrieval product. Future studies based on measurements under constant ozone columns should explore the accuracy of our method in the UV-B spectral range.

### 2.2.2 Aerosol phase functions

We used different aerosol phase functions: for the standard scenario a Henyey–Greenstein (HG) parameterisation with an asymmetry parameter (AP) of 0.68 was used. For further

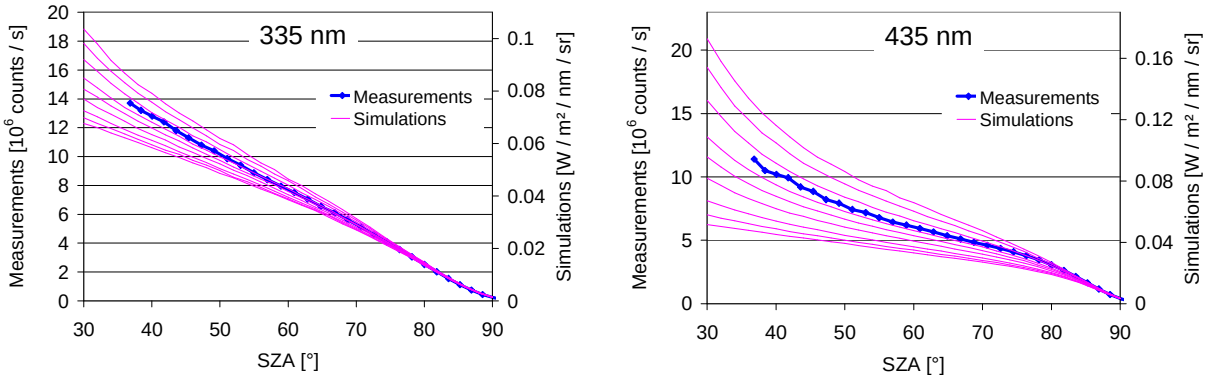


**Figure 5.** Comparison of measured radiances (blue, right axis) with simulated radiances (magenta lines, left axis) for two wavelengths. The lowest simulated radiances are obtained for AOD = 0, and the highest radiances for AOD = 0.5. Results for additional wavelengths are shown in Fig. A3.

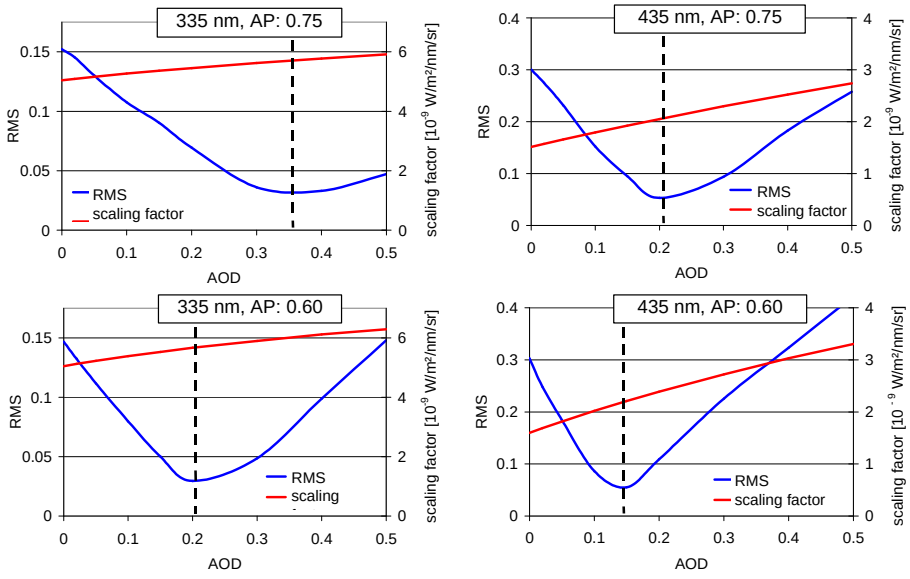


**Figure 6.** Scaling factors and rms derived during the fitting process (Eq. 4) as a function of the AOD for two selected scenarios and wavelengths. The scaling factor is displayed in red (right axis), the rms in blue (left axis). In the upper panel an asymmetry parameter of 0.75, and in the lower panel one of 0.60. is used in the simulations. For both aerosol optical properties the minimum rms of the fit is found for different AOD, but the corresponding scaling factors are almost the same.

scenarios we applied APs of 0.60, 0.75 and 0.85. In addition to the HG phase functions, we used scenarios with Mie-phase functions. They were calculated for log size distributions centred around 500 and 1000 nm. The width of the size distribution (standard deviation) was assumed to be 50 %. The real part of the refractive index was set to 1.34; the imaginary part was set to 0.

### 2.2.3 Surface albedo

The measurement site is surrounded mainly by grassland. Thus for the standard scenario a surface albedo of 0.05 was assumed. In further scenarios we also used values of 0.03, 0.07, and 0.10. To investigate the influence of the changing solar illumination on the surface reflection, we performed simulations for an SZA-dependent surface albedo $\alpha$(SZA). For that purpose we used the parameterisation described in Briegleb et al. (1986):

$$\alpha(\mathrm{SZA}) = \alpha_0 \cdot \frac{1+C}{1+2C \cdot \cos(\mathrm{SZA})}. \quad (3)$$

They suggest a value of $C = 0.40$ for grasslands, while a more recent study by Wang et al. (2007) assumed a smaller value of $C = 0.26$. For our simulations we used the higher value of 0.40 to derive an upper limit of the effect of the changing solar illumination. Here it is interesting to note that

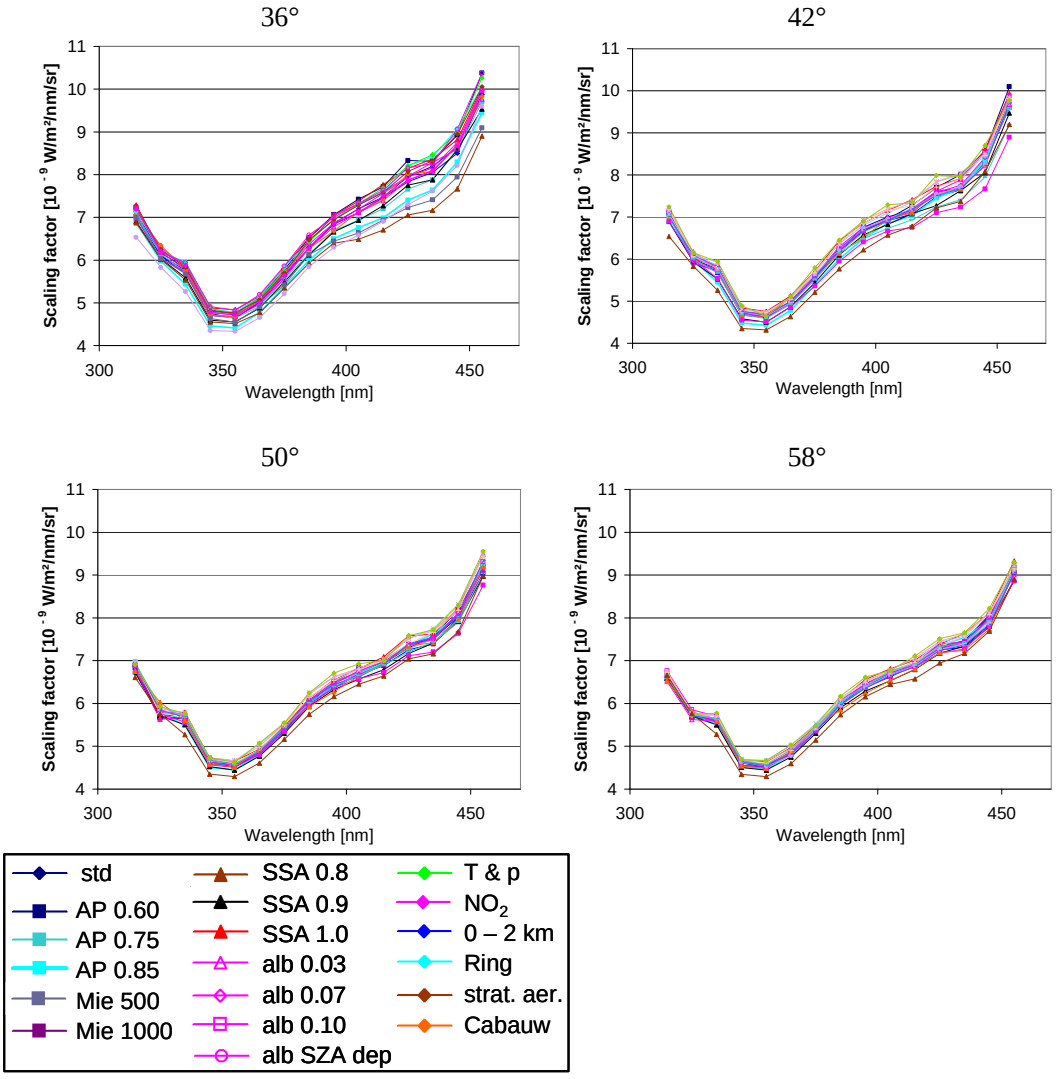


**Figure 7.** Derived scaling factors for different SZA intervals: the lower boundary of the SZA range is varied, while the upper boundary is always 90°. The different lines indicate the results for different scenarios (see Table 1).

the assumption of an SZA-dependent albedo systematically overestimates the effect of the changing solar illumination, because in the considered wavelength range multiple scattering plays an important role. Thus most photons reaching the surface did not directly originate from the sun but were scattered in the atmosphere in this wavelength range. For our simulations we chose $\alpha_0 = 0.0455$ (corresponding to a surface albedo of 0.05 for SZA = 70°).

### 2.2.4 $NO_2$ absorption

At the measurement site rather high $NO_2$ concentrations occurred, which might influence the measured radiances. In addition, the effect of stratospheric $NO_2$ might be important. To investigate the possible effect of the atmospheric $NO_2$ absorption, we defined one scenario including $NO_2$ absorption. From the MAX-DOAS measurements we retrieved a tropospheric $NO_2$ VCD of about $10^{16}$ molecules cm$^{-2}$ during the period of our measurements. For the stratosphere we assumed an $NO_2$ VCD of $3.5 \times 10^{15}$ molecules cm$^{-2}$, based on satellite observations. The tropospheric $NO_2$ layer is assumed to be between the surface and 500 m; the maximum of the stratospheric $NO_2$ is assumed to be at an altitude of 25 km (with a full width at half maximum of 14 km).

### 2.2.5 Stratospheric aerosols

Compared to the aerosols in the boundary layer the optical depth of stratospheric aerosols is usually rather low (except after major volcanic eruptions). Thus we neglected stratospheric aerosols in our simulations. To estimate the potential effect of stratospheric aerosols, we defined an additional sce-

nario including stratospheric aerosols (in a layer between 20 and 30 km altitude with an optical depth of 0.01). We used an HG phase function with an AP of 0.68 and a single-scattering albedo of 1.0.

#### 2.2.6 Temperature and pressure profiles

In our simulations we used temperature and pressure profiles from the US Standard Atmosphere (United States Committee on Extension to the Standard Atmosphere, 1976). To estimate the influence of temperature and pressure variations, we defined an additional scenario using temperature and pressure profiles representative for our measurements obtained from the European Centre for Medium-Range Weather Forecasting (ECMWF). For the time and location of our measurement the pressure (temperature) is about 0.9 % (5 K) larger in the troposphere compared to the US Standard Atmosphere.

## 3 Radiance calibration by fitting measured and simulated radiances

In Fig. 5 the measured radiances (blue lines) are compared to simulated radiances for different AODs (ranging from 0 to 0.5). Measurements and simulation results are displayed as a function of the SZA, but with separate $y$ axes because of their different units (either in counts $s^{-1}$ or in $W\,m^{-2}\,nm^{-1}\,sr^{-1}$). The maxima of both scales are chosen such that measurements and model results are roughly in agreement. It is obvious that not only the absolute values of the simulations but also the curvature of the SZA dependence varies with AOD. This dependence is exploited by our method. The corresponding figures for all selected wavelengths are shown in the Appendix (Fig. A3).

The simulated radiances over the considered SZA range are fitted to the measurements by optimising a scaling factor $S$ until a minimum of the sum of the squared differences between both data sets is reached:

$$\sum_{i=\mathrm{SZA_{min}}}^{\mathrm{SZA_{max}}} [R\,(\mathrm{AOD}, \lambda, i) - S(\lambda) \cdot D\,(\lambda, i)]^2 => \min. \qquad (4)$$

Here $R(\mathrm{AOD}, \lambda, i)$ indicate the simulated radiances at wavelength $\lambda$ for a given AOD, $D(\lambda, i)$ are the values of the detector read-out at wavelength $\lambda$, and $S(\lambda)$ is the scaling factor. The fit is performed separately for the different scenarios, wavelengths and assumed AOD. Examples of the fit results as a function of the AOD for two selected scenarios (top: HG phase function with AP = 0.75; bottom: AP = 0.60) and wavelengths are presented in Fig. 6. The rms shows a clear minimum for a given AOD, indicating that for this AOD the shape of the SZA dependence of the simulated radiances best fits the measurements. For this AOD the derived scaling factor represents the derived absolute calibration of the instrument. Interestingly, similar scaling factors are found for both scenarios, although the minimum rms is found at quite different AOD. This is a very important finding, because it indicates that our method is rather independent from the exact knowledge of the aerosol phase function. In principle also other quantities than the rms could be calculated, e.g. a function decsribing the systematic dependence of the difference between $R$ and $S \cdot D$ (see Eq. 4) as a function of the SZA. But we did not use such an option in this study, because the differences between the derived scaling factors for the different scenarios were found to be rather small (a few percent; see below).

Figure 7 gives an overview on the wavelength dependence of the derived scaling factors. The different graphs show results for different SZA ranges (the lower boundary was varied while the upper boundary was fixed to 90°). The most important conclusions from the results shown in Fig. 7 are that

a. the scaling factors are similar for the different scenarios,

b. the scaling factors are smooth functions of the wavelength.

The first finding indicates that the new calibration method is rather independent from the assumptions on the aerosol properties (and other assumed parameters; see Table 1), confirming the results presented in Fig. 6. The second finding indicates that the statistical uncertainty of the method is rather low.

Interestingly the spread of the results is largest for the largest SZA range (36–90°). This finding first surprised us, because we expected that using more measurements should lead to more stable results. However, the larger variability of the AOD after ∼ 08:00 (corresponding to a SZA of 50°; see Fig. 1) is probably the main cause for the larger differences for the larger SZA interval. Another reason might be that for lower SZA the scattering angle decreases, and thus the influence of the aerosol phase function increases. The fact that those results are most dependent on phase function (Fig. 7a) also seems to point in this direction. In the following we use the SZA range from 50 to 90°.

In Fig. 8 the results for the different scenarios are compared in more detail. The upper panel of Fig. 8a shows ratios of the scaling factors for the different phase functions compared to the standard scenario. The derived scaling factors agree within about 10 %, with decreasing differences towards shorter wavelengths. Also shown are the fit results for the rms (second panel) and the derived AOD (lower panel). While the rms is similar for all phase functions, the AOD shows a large spread. Small AOD (similar to the simultaneous AERONET results) are found for HG phase functions with a small AP (0.60). The highest AOD is retrieved for the HG phase function with an AP of 0.85 and for both Mie phase functions. At 315 and 325 nm the retrieved AOD shows no meaningful results because of the influence of the ozone absorption.

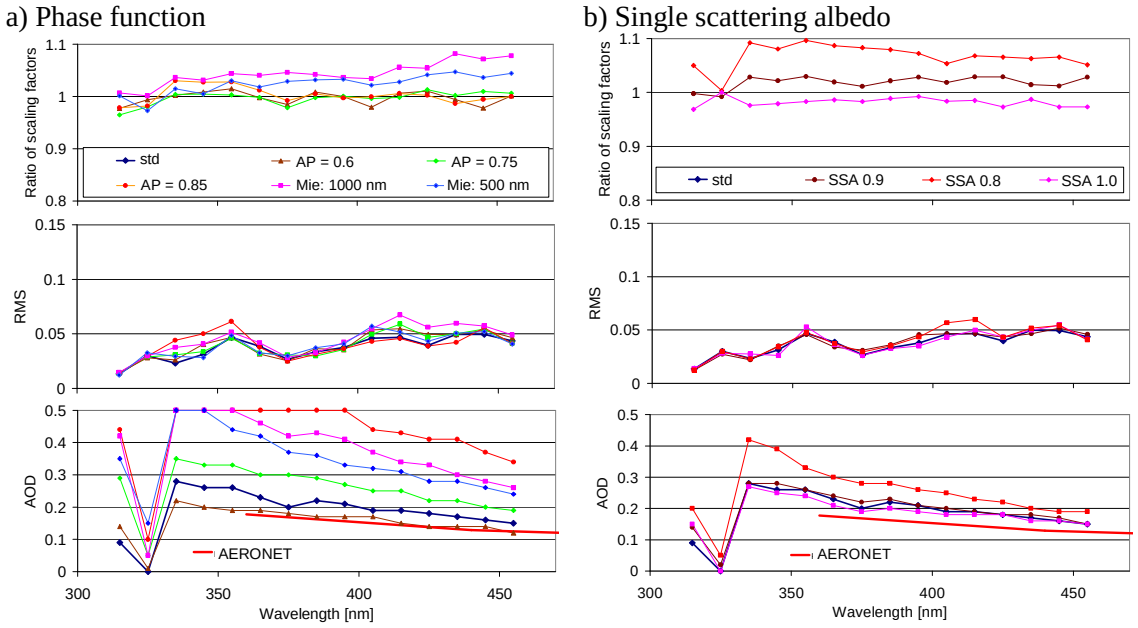


**Figure 8.**

Figure 8b presents results for different aerosol single-scattering albedos. For increasing aerosol absorption decreasing scaling factors are found, but for moderately absorbing aerosols (single scattering albedo $\geq 0.9$) the differences are small ($< 5\,\%$). However, for a strongly absorbing aerosol (single-scattering albedo of 0.8) the derived scaling factors are about 5–10 % smaller compared to the standard scenario. Thus if during the measurements such strongly absorbing aerosols are present, the derived scaling factors would be by 5–10 % too small if less absorbing aerosols were assumed in the radiative transfer simulations. Fortunately, such cases could be easily identified by the large deviation of the simultaneously determined AODs from the AODs derived from sun photometers. Also the rms is slightly larger.

In Fig. 8c the effect of varying the surface albedo is shown. Again very small variations of the derived scaling factors, rms and AOD, are found. Interestingly, for the scenario with the SZA-dependent albedo, the largest rms is derived. This finding might indicate that the assumed SZA dependence indeed overestimates the influence of the changing solar illumination (see Sect. 2.2.3).

Figure 8d shows results for different atmospheric parameters (see Table 1). The effects of aerosol layer height, temperature and pressure profiles, stratospheric aerosols, and $NO_2$ absorption have again a rather small effect on the derived scaling factors, rms and AOD. Here it is interesting to note that the effect of a combined change of temperature and pressure is slightly smaller than the effects of individual changes of pressure and temperature (not shown). Nevertheless, they are still small compared to other uncertainties. The scenario referred to as "Cabauw" includes at the same time several changes compared to the standard scenario: temperature and pressure profiles are taken for the day of the measurements, and also stratospheric aerosols and $NO_2$ absorption are included. In addition, Raman scattering is considered. This scenario probably best describes the atmospheric conditions during our measurements. The effect of the combined changes of the Cabauw scenario on the scaling factors compared to the standard scenario is still small ($< 5\,\%$).

In Fig. 8e we show the effect of polarisation and rotational Raman scattering. The influence of rotational Raman scattering on the scaling factors is very small ($< 2\,\%$). The largest deviations occur – as expected – for wavelengths close to strong spectral variations of the solar irradiance (see Fig. 2). In contrast, the neglect of polarisation has a rather strong effect on the fit results (see also Mishchenko et al., 1994): much lower scaling factors and much higher rms and AOD compared to the standard scenario are derived.

Figure 9 presents an example of a calibrated radiance spectrum measured at 06:54 (SZA = 61°) based on the scaling factors for the Cabauw scenario. Unfortunately, we have no possibility for a direct comparison to another radiance spectrum measured at the same location and time. But in a publication by Seckmeyer et al. (2009) we found radiance spectra measured in zenith direction under similar atmospheric conditions (clear sky; SZA = 62°) on 2 May 2007 in Hanover, Germany. Unfortunately, the raw data of those spectra are no longer available. Thus we graphically copied a radiance spectrum (for a SZA of 62°) from the original figure in Seckmeyer et al. (2009) and overlaid it on our calibrated spectrum. Note that the measurement in Hanover was scaled by a factor of 0.97 to account for the effect of the slightly dif-

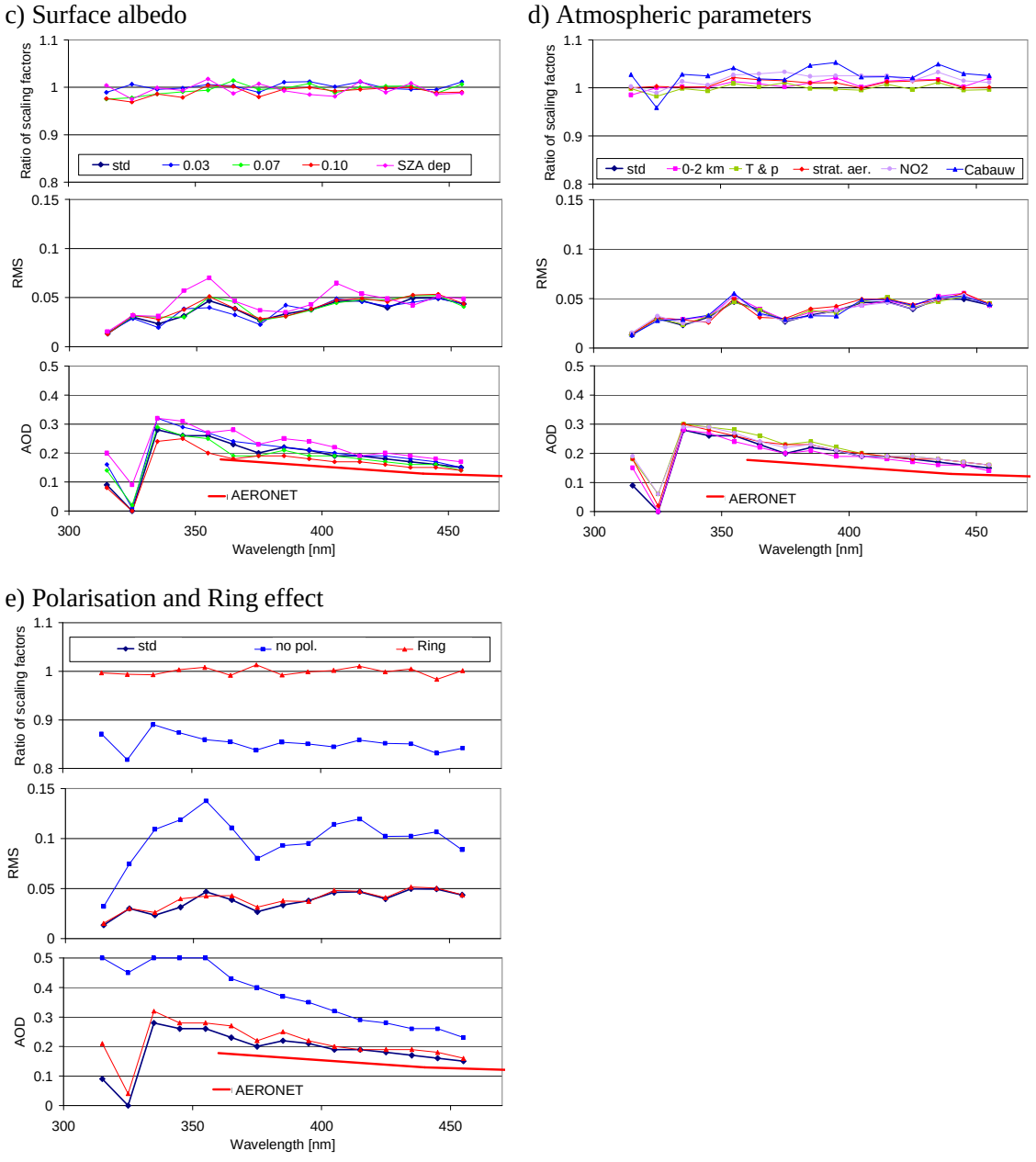


**Figure 8.** Comparison of the derived scaling factors, rms and AOD, for different scenarios (the scaling factors for the standard scenario are divided by the scaling factors for the different scenarios; see Table 1).

ferent viewing geometries (exact zenith view, compared to 85° elevation angle of our measurement). For wavelengths > 335 nm our radiance spectrum agrees very well with the radiance spectrum measured at Hanover. Note that the sun–earth distance during the measurements in Hanover was almost the same as in our measurements (0.3 % difference). Also the AOD and the ozone column were similar: the AOD at 550 nm derived from MODIS TERRA is about 0.15 (obtained via the NASA Giovanni website: http://giovanni.sci.gsfc.nasa.gov/giovanni/). The ozone column density derived from OMI was about 330 DU (obtained from the TEMIS website: http://temis.nl/index.php).

### 3.1 Comparison with AERONET

During the fit process not only the scaling factor for the absolute calibration is determined, but also the AOD (see Figs. 6 and 8). The choice of the aerosol phase function has the strongest effect on the retrieved AOD, while other parameters (see Table 1) have only a small influence. Very good agree-

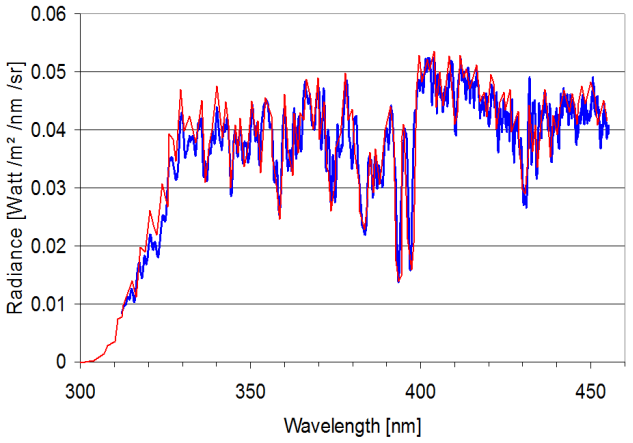


**Figure 9.** Comparison of a calibrated spectrum (blue), measured on 24 June 2009 at 06:54, at a SZA of 61°, and an independent measurement under similar conditions (red) on 2 May 2007 in Hanover, Germany (clear sky; SZA: 62°; Seckmeyer et al., 2009). The measurement in Hanover was scaled by a factor of 0.97 to account for the effect of the slightly different viewing geometries (exact zenith view, compared to 85° elevation angle of our measurement).

ment with AERONET AOD is found for the scenario with an aerosol asymmetry parameter of 0.60. Large deviations are found for HG phase functions with an AP of 0.85 and both Mie phase functions. Also the neglect of polarisation leads to unrealistically high AOD.

The comparison to the AERONET results is very useful, because it allows an independent assessment of the results of the new method. Furthermore, based on the comparison to the AERONET AOD, the uncertainties of the new calibration method (see Fig. 6) can be further reduced, because scenarios with unrealistic AOD results can be simply disregarded. Here it should be noted that the retrieved AOD for wavelengths < 330 nm are not meaningful for our measurements because of the strong change of the ozone layer during the measurements (see Figs. 3 and 4). Disregarding the scenarios with the largest deviations of the AOD from the AERONET measurements, from the sensitivity analyses presented in Fig. 8 we estimate the uncertainty of our calibration method to be < 6 %.

## 4 Conclusions

We presented a new method for the calibration of UV–vis instruments that measure the spectrally resolved sky radiance, for example zenith sky DOAS instruments or MAX- DOAS instruments. Our method does not rely on laboratory measurements but is based on the comparison of the solar zenith angle dependence of the measured zenith sky radiance with results from radiative transfer simulations. The prerequisites for the application of our method are that the sky be clear and the aerosol optical depth be constant and low for a period of a few hours. At best, even further aerosol properties like the single-scattering albedo or the asymmetry parameter are known. This would allow the number of scenarios used for the calibration to be reduced. For observations at short wavelengths, also the thickness of the ozone layer should be constant (and known) during the measurements. We selected measurements during a period of about 4 h covering a SZA range between 50 and 90°.

Apart from being a simple and cheap procedure, another advantage of our method is that the calibration is derived directly from the atmospheric spectra; thus the occurrence of potential changes of the instrument during the transport from the laboratory to the field can be neglected. The radiometric calibration can be determined for individual wavelengths; in this study we selected wavelengths in intervals of 10 nm between 315 and 455 nm (the wavelength range of our instrument). The calibration function was found to be spectrally smooth and can therefore be interpolated (if the intervals are not chosen too large). Alternatively, also additional wavelengths in between the chosen wavelengths could be used.

From our method also the aerosol optical depth for the selected wavelengths is determined. The comparison of the derived AOD with AOD derived from AERONET observations can be used to assess the quality of the calibration results. In particular, scenarios yielding unrealistic AOD values can be removed. If we do not take into account scenarios which yield unrealistically high AOD, the variation of the derived calibration results is further reduced. From the sensitivity studies based on different scenarios, we estimate the uncertainty of our method to be < 7 % (including the uncertainties of the solar irradiance measurement). Here it should be noted that for larger AOD larger uncertainties should probably be expected. This aspect should be investigated in future studies.

Our results clearly indicate that the radiative transfer simulations have to consider polarisation. In contrast, the effect of rotational Raman scattering can be neglected.

Our new method is of importance to many applications, including the determination of actinic fluxes, the characterisation of aerosol and cloud properties or the quantification of the shortwave radiative flux at the position of the instrument. Another interesting application might be the quantification of the yield of photovoltaic cells. For wavelengths below about 330 nm it is essential that the ozone column density during the measurements be constant and known. The accuracy of our method in the UV-B spectral range should be further explored in future studies based on measurements under constant ozone layer thickness during the period of the measurements.

## Appendix A

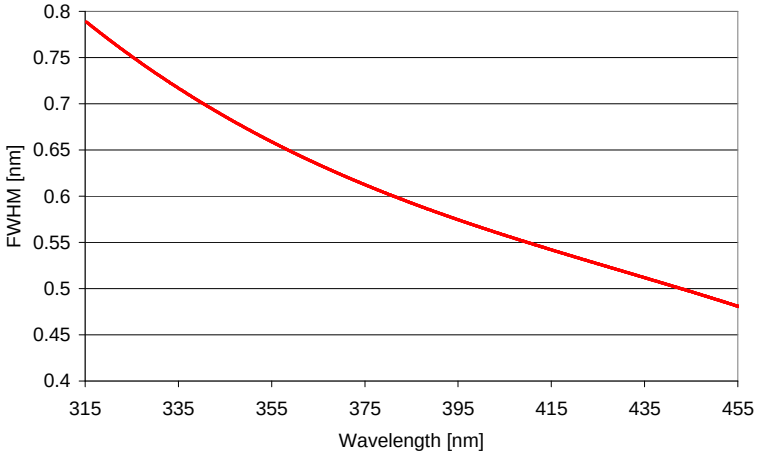


**Figure A1.** Spectral resolution (full width at half maximum, FWHM) as a function of wavelength determined from a fit to a high-resolution solar spectrum.

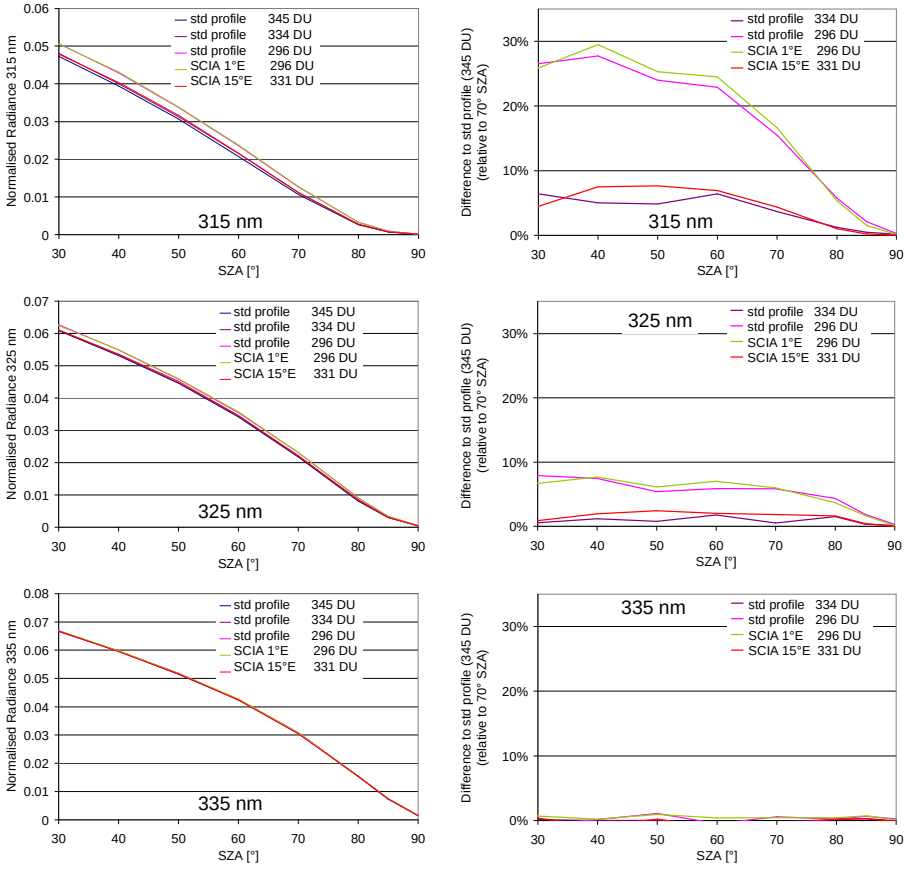


**Figure A2.** Left: simulated radiances for the different $O_3$ profiles shown in Fig. 3. The profiles differ in shape and $O_3$ VCD. Right: relative differences of the radiances compared to the standard profile (345 DU) (the radiance differences are divided by the radiances at SZA = 70°).

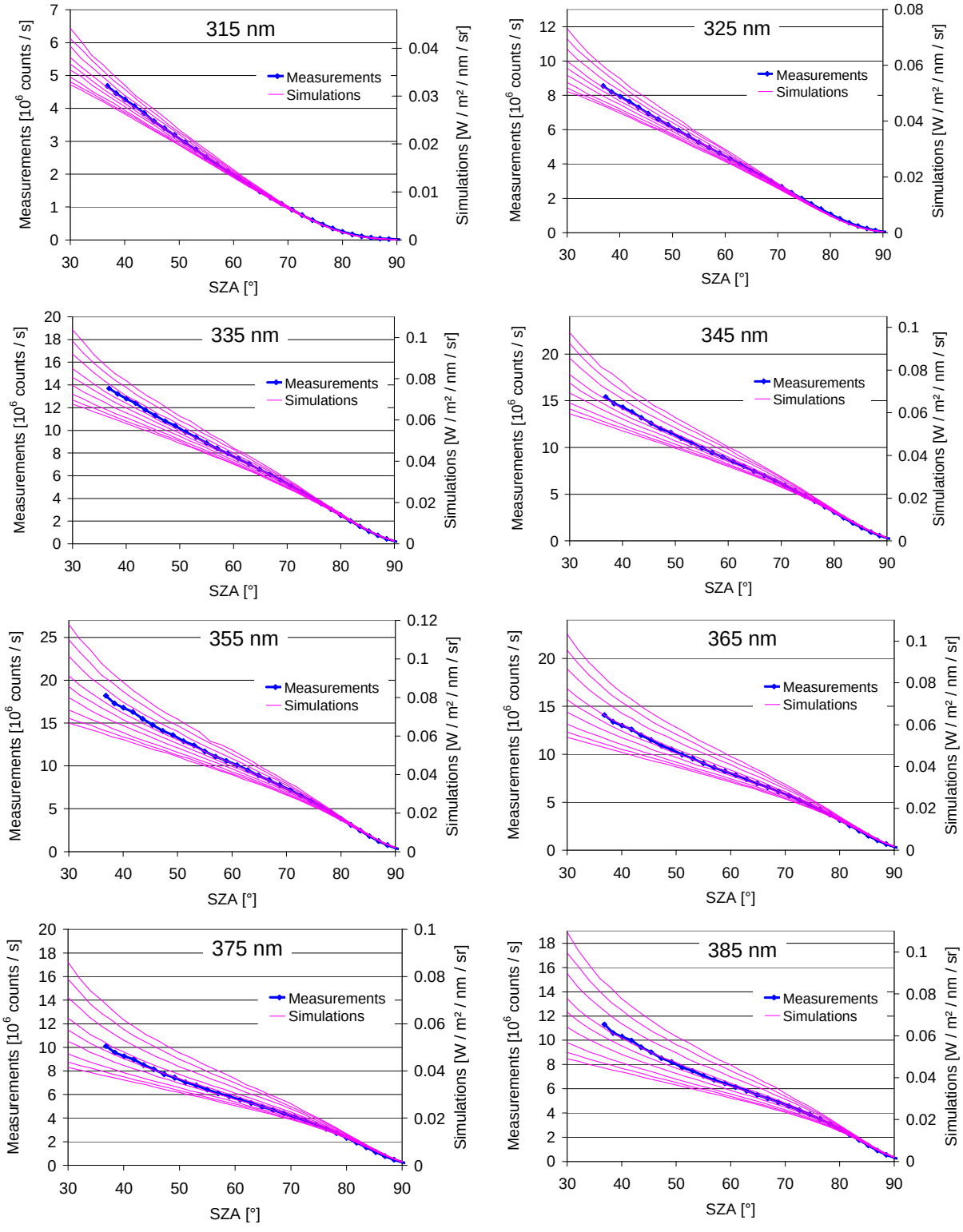
315 nm
325 nm
335 nm
345 nm
355 nm
365 nm
375 nm
385 nm
Measurements
Simulations
Measurements [10^6 counts / s]
Simulations [W / m² / nm / sr]
SZA [°]

**Figure A3.**

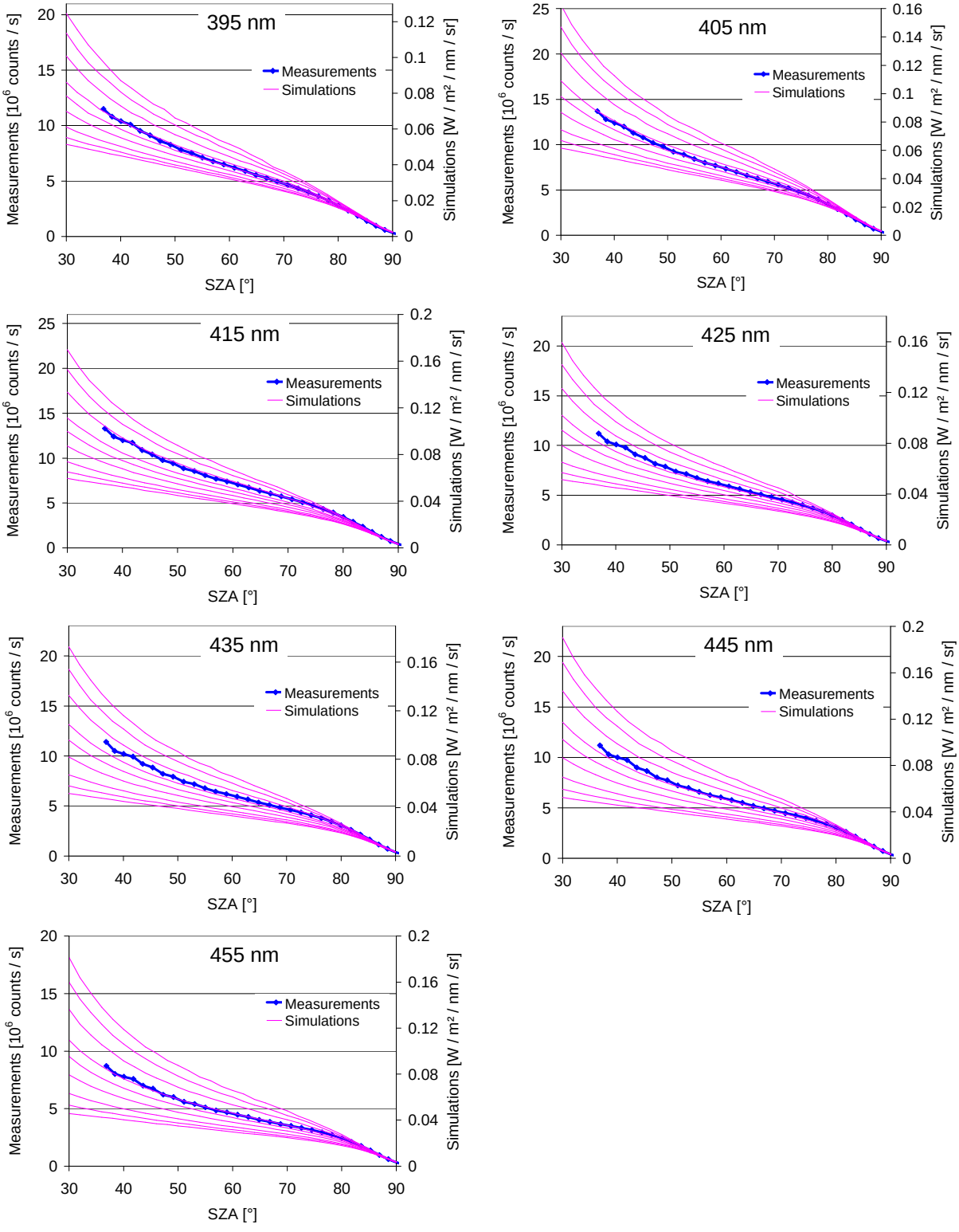


**Figure A3.** Comparison of measured radiances (blue, right axis) with simulated radiances (magenta lines, left axis) for all wavelengths used in our study. The lowest simulated radiances are obtained for AOD = 0, and the highest radiances for AOD = 0.5.

*Acknowledgements.* We want to thank the organisers of the Cabauw Intercomparison Campaign of Nitrogen Dioxide measuring Instruments (CINDI) in summer 2009 (http://www.knmi.nl/samenw/cindi/), especially Ankie Piters and Marc Kroon. We thank J. S. (Bas) Henzing and his staff for their effort in establishing and maintaining the Cabauw AERONET site used in this investigation. The radiance measurements at Hanover (Fig. 9) were copied from a publication by Seckmeyer et al. (2009). We used the Monte Carlo Radiative Transfer Inversion Model (McArtim), which was developed by T. Deutschmann.

The article processing charges for this open-access publication were covered by the Max Planck Society.

Edited by: A. Hofzumahaus

## References

Bernhard, G., Booth, C. R., and Ehramjian, J. C.: Version 2 data of the National Science Foundation's Ultraviolet Radiation Monitoring Network: South Pole, J. Geophys. Res., 109, D21207, doi:10.1029/2004JD004937, 2004.

Briegleb, B. P., Minnis, P., Ramanathan, V., and Harrison, E.: Comparison of regional clear sky albedos inferred from satellite observations and model calculations, J. Clim. Appl. Meteorol., 25, 214–226, 1986.

Chance, K. and Kurucz, R. L.: An improved high-resolution solar reference spectrum for Earth's atmosphere measurements in the ultraviolet, visible, and near infrared, J. Quant. Spectrosc. Ra., 111, 1289–1295, 2010.

Chance, K. and Spurr R. J. D.: Ring effect studies: Rayleigh scattering, including molecular parameters for rotational Raman scattering, and the Fraunhofer spectrum, Appl. Optics, 36, 5224–5230, 1997.

Deutschmann, T., Beirle, S., Frieß, U., Grzegorski, M., Kern, C., Kritten, L., Platt, U., Pukite, J., Wagner, T., Werner, B., and Pfeilsticker, K.: The Monte Carlo Atmospheric Radiative Transfer Model McArtim: Introduction and Validation of Jacobians and 3D Features, J. Quant. Spectr. Rad. Transf., 112, 1119–1137, doi:10.1016/j.jqsrt.2010.12.009, 2011.

Götz, F. W. P., Meetham, A. R., and Dobson, G. M. B.: The vertical distribution of ozone in the atmosphere, P. Roy. Soc. Lond. A Mat., 145, 416–446, 1934.

Haigh, J. D., Winning, A. R., Toumi, R., and Harder, J. W.: An influence of solar spectral variations on radiative forcing of climate, Nature, 467, 696–699, doi:10.1038/nature09426, 2010.

Hönninger G. and Platt, U.: Observations of BrO and its vertical distribution during surface ozone depletion at Alert, Atmos. Environ., 36, 2481–2490, 2002.

Landgraf, J., Hasekamp, O. P., van Deelen, R., and Aben, I.: Rotational Raman scattering of polarized light in the Earth atmosphere: a vector radiative transfer model using the radiative transfer perturbation theory approach, J. Quant. Spectrosc. Ra., 87, 399–433, 2004.

Loyola, D. G., Koukouli, M. E., Valks, P., Balis, D. S., Hao, N., Van Roozendael, M., Spurr, R. J. D., Zimmer, W., Kiemle, S., Lerot, C., and Lambert, J.-C.: The GOME-2 total column ozone product: Retrieval algorithm and ground-based validation, J. Geophys. Res., 116, D07302, doi:10.1029/2010JD014675, 2011.

Mishchenko, M. I., Lacis, A. A., and Travis, L. D.: Errors induced by the neglect of polarisation in radiance calculations for Rayleigh-scattering atmospheres, J. Quant. Spectrosc. Ra., 51, 3, 491–510, 1994.

Piters, A. J. M., Boersma, K. F., Kroon, M., Hains, J. C., Van Roozendael, M., Wittrock, F., Abuhassan, N., Adams, C., Akrami, M., Allaart, M. A. F., Apituley, A., Beirle, S., Bergwerff, J. B., Berkhout, A. J. C., Brunner, D., Cede, A., Chong, J., Clémer, K., Fayt, C., Frieß, U., Gast, L. F. L., Gil-Ojeda, M., Goutail, F., Graves, R., Griesfeller, A., Großmann, K., Hemerijckx, G., Hendrick, F., Henzing, B., Herman, J., Hermans, C., Hoexum, M., van der Hoff, G. R., Irie, H., Johnston, P. V., Kanaya, Y., Kim, Y. J., Klein Baltink, H., Kreher, K., de Leeuw, G., Leigh, R., Merlaud, A., Moerman, M. M., Monks, P. S., Mount, G. H., Navarro-Comas, M., Oetjen, H., Pazmino, A., Perez-Camacho, M., Peters, E., du Piesanie, A., Pinardi, G., Puentedura, O., Richter, A., Roscoe, H. K., Schönhardt, A., Schwarzenbach, B., Shaiganfar, R., Sluis, W., Spinei, E., Stolk, A. P., Strong, K., Swart, D. P. J., Takashima, H., Vlemmix, T., Vrekoussis, M., Wagner, T., Whyte, C., Wilson, K. M., Yela, M., Yilmaz, S., Zieger, P., and Zhou, Y.: The Cabauw Intercomparison campaign for Nitrogen Dioxide measuring Instruments (CINDI): design, execution, and early results, Atmos. Meas. Tech., 5, 457–485, doi:10.5194/amt-5-457-2012, 2012.

Pissulla, D., Seckmeyer, G., Cordero, R. R., Blumthaler, M., Schallhart, B., Webb, A., Kift, R., Smedley, A., Bais, A. F., Kouremeti, N., Cede, A., Hermang, J., and Kowalewskig, M.: Comparison of atmospheric spectral radiance measurements from five independently calibrated systems, Photochem. Photobio. S., 8, 516–527, 2009.

Platt, U. and Stutz, J.: Differential Optical Absorption Spectroscopy, Principles and Applications, Springer, Berlin, Germany, 2008.

Roscoe, H. K., Van Roozendael, M., Fayt, C., du Piesanie, A., Abuhassan, N., Adams, C., Akrami, M., Cede, A., Chong, J., Clémer, K., Friess, U., Gil Ojeda, M., Goutail, F., Graves, R., Griesfeller, A., Grossmann, K., Hemerijckx, G., Hendrick, F., Herman, J., Hermans, C., Irie, H., Johnston, P. V., Kanaya, Y., Kreher, K., Leigh, R., Merlaud, A., Mount, G. H., Navarro, M., Oetjen, H., Pazmino, A., Perez-Camacho, M., Peters, E., Pinardi, G., Puentedura, O., Richter, A., Schönhardt, A., Shaiganfar, R., Spinei, E., Strong, K., Takashima, H., Vlemmix, T., Vrekoussis, M., Wagner, T., Wittrock, F., Yela, M., Yilmaz, S., Boersma, F., Hains, J., Kroon, M., Piters, A., and Kim, Y. J.: Intercomparison of slant column measurements of $NO_2$ and $O_4$ by MAX-DOAS and zenith-sky UV and visible spectrometers, Atmos. Meas. Tech., 3, 1629–1646, doi:10.5194/amt-3-1629-2010, 2010.

Seckmeyer, G., Smolskaia, I., Pissulla, D., Bais, A. F., Tourpali, K., Meleti, C., and Zerefos, C.: Solar UV: measurements and trends, in: Twenty Years of Ozone Decline, Proceedings of the Symposium for the 20th Anniversary of the Montreal Protocol, Athens, 23–26 September 2007, edited by: Zerefos, C., Contopoulos, G. and Skalkeas, G., Part VI, Springer, the Netherlands, 359–368, 2009.

Sonkaew, T., Rozanov, V. V., von Savigny, C., Rozanov, A., Bovensmann, H., and Burrows, J. P.: Cloud sensitivity studies for stratospheric and lower mesospheric ozone profile retrievals from mea-

surements of limb-scattered solar radiation, Atmos. Meas. Tech., 2, 653–678, doi:10.5194/amt-2-653-2009, 2009.

Thuillier, G., Floyd, L., Woods, T. N., Cebula, R., Hilsenrath, E., Herse, M., and Labs, D.: Solar irradiance reference spectra. in: Solar Variability and its Effect on the Earth's Atmosphere and Climate System, edited by: Pap, J. M., AGU, Washington, DC, USA, 171–194, 2004.

United States Committee on Extension to the Standard Atmosphere: US Standard Atmosphere, 1976, National Oceanic and Atmospheric Administration, National Aeronautics and Space Administration, United States Air Force, Washington, DC, USA, 1976.

Wagner, T., Apituley, A., Beirle, S., Dörner, S., Friess, U., Remmers, J., and Shaiganfar, R.: Cloud detection and classification based on MAX-DOAS observations, Atmos. Meas. Tech., 7, 1289–1320, doi:10.5194/amt-7-1289-2014, 2014.

Wang, Z., Zeng, X., and Barlage, M.: Moderate resolution imaging spectroradiometer bidirectional reflectance distribution function–based albedo parameterization for weather and climate models, J. Geophys. Res., 112, D02103, doi:10.1029/2005JD006736, 2007.

Wuttke, S., Seckmeyer, G., Bernhard, G., Ehramjian, J., McKenzie, R., Johnston, P., and O'Neil, M.: New spectroradiometers complying with the NDSC standards, J. Atmos. Ocean. Tech., 23, 241–251, 2006.